Extending the Linearity of AlScN Contour-Mode-Resonators through Acoustic Metamaterials-based Reflectors

Xuanyi Zhao¹, Onurcan Kaya¹, Michele Pirro¹, Pietro Simeoni¹, Jeronimo Segovia-Fernandez², and Cristian Cassella¹

¹Department of Electrical and Computer Engineering, Northeastern University ²Kilby Labs, Texas Instruments

Abstract—This work describes the implementation of acoustic metamaterials (AMs) made of a forest of rods at the sides of a suspended Aluminum Scandium Nitride (AlScN) contour-moderesonator (CMR) to increase its power handling without causing degradations of its electromechanical performance. The increase in usable anchoring perimeter with respect to conventional CMRdesigns, enabled by the adoption of two AMs-based lateral anchors, permits to achieve an improved heat conduction from the resonator's active region to the substrate. Furthermore, thanks to such AMs-based lateral anchors' unique acoustic dispersion features, the attained increase of anchored perimeter does not cause any degradations of the CMR's electromechanical performance, even leading to a $\sim 15\%$ improvement in the measured quality factor. Finally, we experimentally show that using our AMs-based lateral anchors leads to a more linear CMR's electrical response, which is enabled by a $\sim 32\%$ reduction of its Duffing nonlinear coefficient with respect to the corresponding value attained by a conventional CMR-design that uses fully-etched lateral sides.

Index Terms—Acoustic Metamaterials, Aluminum Scandium Nitride, Two-Dimensional-Resonant-Rods, Acoustic Reflectors, Thermal Linearity, Quality Factor

I. INTRODUCTION

In the last decades, Aluminum Nitride (AlN) acoustic resonators have been developed and used for a broad range of applications, including frequency generation, timing, filtering, sensing, self-interference cancellation, and more [1]-[8]. In particular, AlN Contour Mode Resonators (CMRs) [3], [4], [9]–[11] have shown superior lithographic frequency tunability in a CMOS-compatible fabrication process, allowing to monolithically integrate multiple resonators with different resonance frequencies (f_{res}). CMRs are formed by a piezoelectric film sandwiched between two metal layers. Each CMR's suspended plate is generally connected to the substrate through two anchors placed along the in-plane direction (e.q., the vdirection) that is orthogonal to the main vibrational direction (e.g., the x-direction). Such anchors, referred to as y-anchors, generally present a narrow width (even lower than halfwavelength, $\lambda/2$) to minimize the amount of acoustic energy leaking into the substrate. The mitigation of such energy leakage is key to prevent any reduction of the resonator's quality factor (Q_s) [12], [13]. However, due to the requirement of narrow y-anchors to maximize Q_s , the power handling

of CMRs becomes primarily limited by thermally-induced Duffing nonlinearity [14]. Moreover, the use of thin-film AlN with relatively low thermal conductivity exacerbates this nonlinear phenomenon [15]–[18]. Consequently, a trade-off exists, for CMRs, between power handling and maximum attainable Q_s (and $FoM = k_t^2 \cdot Q_s$, being k_t^2 the electromechanical coupling coefficient) [19]-[22]. In recent years, the use of Scandium-doped Aluminum Nitride (AlScN) in microacoustic piezoelectric resonators has been largely investigated to boost the k_t^2 of the AlN counterparts [23]–[25]. Such a large interest is justified by the superior piezoelectric strength of AlScN in comparison to AlN. Yet, AlScN presents a thermal conductivity that is up to two orders of magnitude lower than AlN [26]–[29]. As a result, all the existing AlScN resonators, including AlScN CMRs, are much more susceptible to Duffing nonlinearity than the AlN counterparts, inherently exhibiting lower power handling. This represents a huge limitation when using AlScN CMRs in filters, since it causes distortion and loss of information, and in oscillators, since it directly impacts frequency stability. Therefore, it is necessary to find novel design features that enable improved thermal dissipations in AlScN resonators without compromising their achievable Q_s .

Recently, our group has reported a series of works on acoustic metamaterials (AMs) formed by arrays of AlN and AlScN locally-resonant rods. Such AMs present unique acoustic properties since they are designed to have specific dispersion characteristics that alternate acoustic passbands and stopbands within a desired range of frequencies. For instance, we demonstrated piezoelectric AMs-based devices embodying a forest of resonant rods designed to suppress any highorder Lamb waves via a stopband, increasing the mechanical energy of two-dimensional modes of vibration piezoelectrically transduced in all the rods. These devices constitute a new class of Bulk-Acoustic-Wave (BAW) resonators, namely the Two-Dimensional-Resonant-Rods (2DRRs). 2DRRs are characterized by a considerably larger k_t^2 than other AlN or AlScN resonators operating within the same band [30]–[33]. In a separate demonstration, we also showed that the same AMs can be used to form acoustic delay lines, offering wide fractional bandwidths and high group delays enabled by the slow-wave propagation characteristics of the AMs-based structure. [34]-[36].

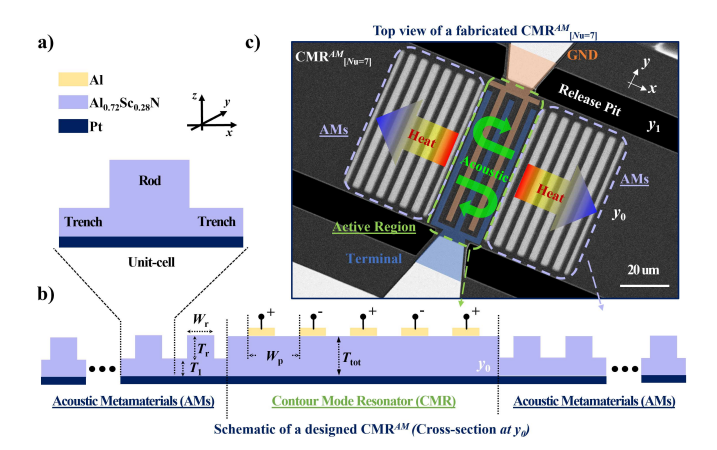


Fig. 1. (a) Cross-sectional view of the unit-cell of the reported AMR, consisting of an AlScN rod on top of a thin Pt/AlScN plate. (b) Cross-sectional view of a CMR with a pair of AMRs attached along their two lateral sides. (c) Scanned electron microscope (SEM) picture of a fabricated CMR^{AM} using two AMRs, each formed by seven unit-cells.

In this work, we describe the use of AMs to form compact frequency-selective reflective anchors, from now on labeled as Acoustic Metamaterials-based Reflectors (AMRs, Figure 1). We show how using such AMRs along the lateral edges of an AlScN CMR, in combination with conventional narrow *y-anchors*, permits to confine the acoustic energy within the resonator's active region while ensuring a much larger anchoring perimeter than conventional CMR-designs. As a result, AMRs provide a substantial release path for the heat generated in the resonator's active region, mitigating the thermal nonlinearities with respect to conventional, laterally-etched AlScN CMRs. Figure 1 illustrates our idea by showing a fabricated Al_{0.72}Sc_{0.28}N CMR attached to substrate via both *y-anchors* and AMRs.

II. PRINCIPLE OF OPERATION

This section discusses the operation of CMRs using AMRs along their lateral sides (CMR^{AM}) and explains why using AMRs permits to overcome the trade-off that currently exists in the design of CMRs between anchor losses and power handling. We first provide a review of the CMR-technology. Then, we outline the operational principle of AMRs. Finally, we compare CMR^{AM} with CMRs using planar metal reflectors (MRs) along their lateral sides through a Finite Element Methods (FEM) investigation.

A. CMRs, Anchor Losses and Thermal Nonlinearities

In their most used design topology, CMRs are formed by a piezoelectric plate sandwiched between one interdigitated metal structure (IDT) and a floating metal plate. The IDT-structure is responsible for the transduction of a longitudinal mode of vibration from its generated electric field in the piezoelectric plate. In particular, when relying on c-oriented hexagonal AlN thin-films, CMRs excite a longitudinal mode of vibration noted as contour-mode in their suspended membrane, which coincide with the S_0 Lamb-wave mode in the limit of λ -being much larger than the CMRs' thickness. In order

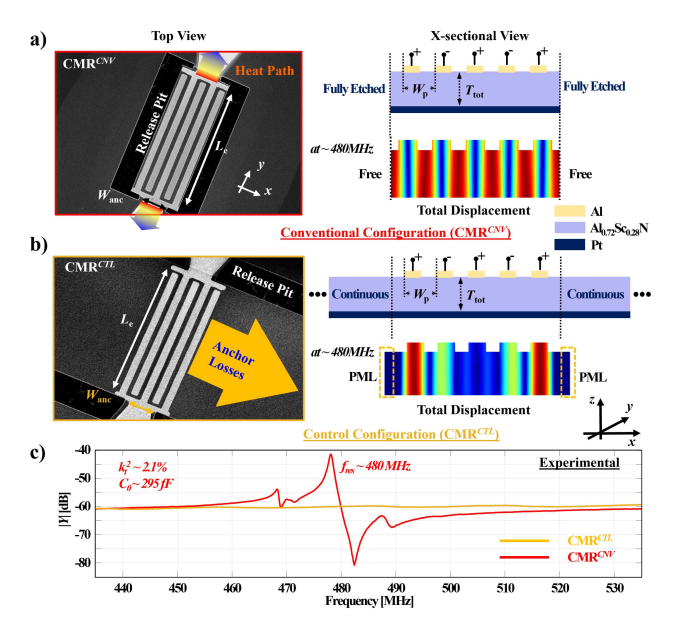


Fig. 2. a) SEM picture and schematic cross-sectional view of a conventional CMR design uniquely supported by two narrow *y-anchors* (dubbed as CMR^{CNV}); b) SEM picture and schematic cross-sectional view of a CMR design with un-etched lateral sides (dubbed as CMR^{CTL}); c) A comparison of the measured admittance response for CMR^{CNV} (in red) and CMR^{CTL} (in yellow).

to piezoelectrically transduce such contour-mode, a standing wave must form within CMRs' active region and along CMRs' lateral direction. Usually, such transduction requires the lateral boundaries of the membrane to be cut-off and the structure to be suspended in order to prevent the generated acoustic wave from leaking into the substrate. In fact, when looking at the electrical response of a conventional CMR with or without such etched lateral sides, one would immediately notice that Q_s becomes too small for even being able to electrically detect any resonance if such sides are left fully-attached to the substrate (Figure 2). As a result, CMRs have historically recurred to fully-etched lateral sides despite the fact that only having the y-anchors to structurally support them heavily shrinks the path available for the heat generated upon vibration to flow into the substrate. In fact, CMRs' rate of heat-flow into the substrate is inversely proportional to an equivalent thermal resistance (R_{th}) that grows as lower anchoring perimeters are used. Larger R_{th} values relate to larger temperature increases in the CMRs' body, which in turn induces larger thermal nonlinearities and degrades CMRs' power handling [14]. It is worth noting that relying on a passive temperature compensation is one method that can be utilized to limit the impact of thermal nonlinearities in CMRs [37], but this method often comes with degradations of CMRs' electromechanical performance. Moreover, while using AlScN offers a significant performance improvement in terms of k_t^2 with respect to AlN, this material is characterized by a thermal conductivity that is up to two orders of magnitude smaller than AlN [29]. As a result, for any selected anchoring strategy, AlScN CMRs exhibit significantly worse thermal linearity than their AlN counterparts. This represents a huge challenge that is calling for new AIScN CMR-designs granting

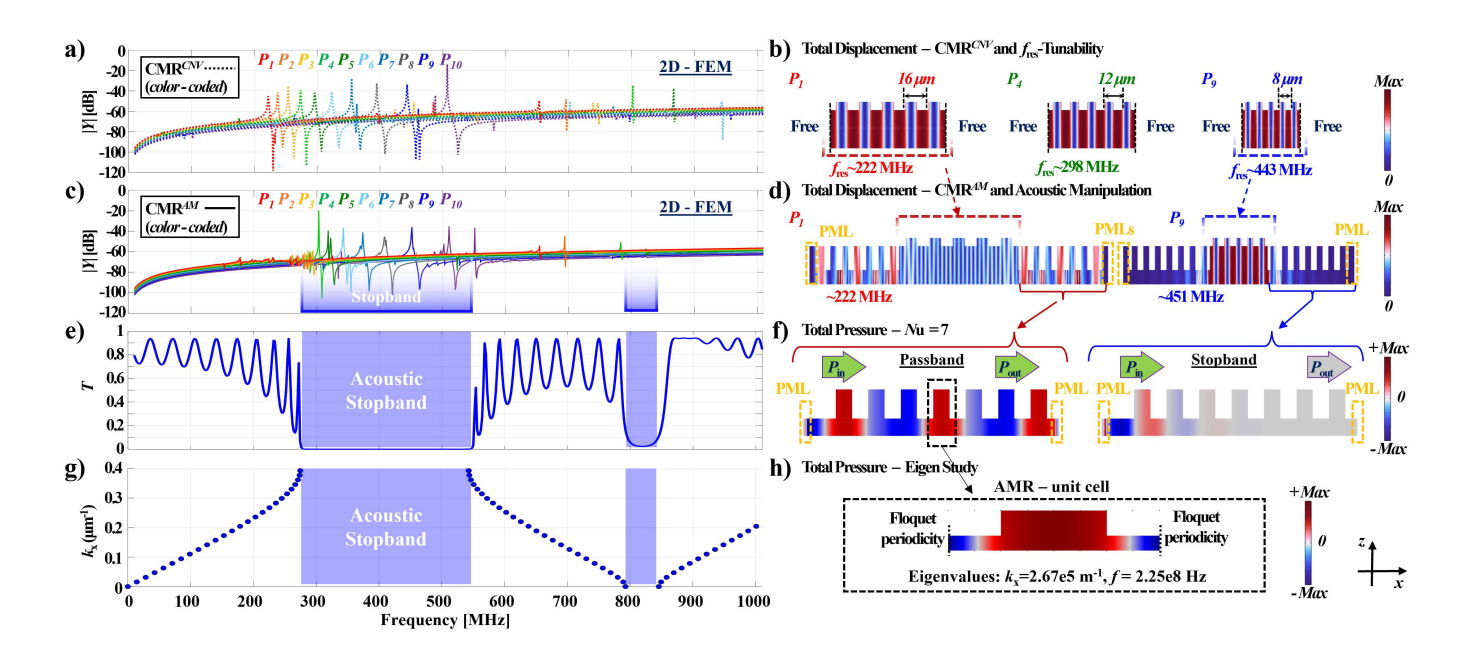


Fig. 3. FEM-analysis of CMR-designs with different W_p values when using fully-etched lateral sides [dubbed as CMR^{CNV}, see (a-b)] or alternatively, when using two AMRs attached to the CMRs' lateral sides [dubbed as CMR^{AM}, see (c-d)]. In a) the admittance magnitude of the different analyzed CMR^{CNV}-devices is reported; in b) the at-resonance total displacement modeshape for CMR^{CNV}-devices using three different W_p values is reported; in c) the admittance magnitude of the different analyzed CMR^{AM}-devices is reported; in (d) the at-resonance total displacement modeshape for CMR^{AM}-devices using two different W_p values is reported; in e) the acoustic transmission (T) for the AMRs used by the CMR^{AM}-devices used in (d) is plotted vs. frequency; in f) the total pressure distribution extracted from the FEM simulation we run to extract (e) is plotted for two different frequencies, within or outside of the widest AMRs' BG; in g) the lateral wavevector (k_x) for the contour-mode in the AMRs is plotted vs. frequency, showing the existance of two BGs; in h) schematic cross-sectional view of unit-cell and boundary-conditions used during the FEM extraction of (g).

improved thermal linearity without affecting the achievable electromechanical performance. The nature of this challenge unfolds as we realize that the acoustic motion to be leveraged and the heat accumulation in CMRs' body to be minimized are both originated from elastic vibrations. Meanwhile, the complex ballistic process of heat and acoustic phonons that may impair the heat conduction only occurs when the characteristic dimension of the vibrating structure becomes smaller than the mean free path (MFP) of heat phonons. Therefore, when analyzing CMRs' ability to dissipate heat, we can reasonably treat the heat conduction from CMRs' active regions into the substrate as a diffusive process which obeys Fourier's law [29], [38]–[40]. Such assumption helps us largely simplify the investigation and helps us lay out our design strategy. In fact, to improve the thermal linearity of CMRs we just need to increase the total anchoring perimeter, and finding ways to introduce anchors even along the lateral directions represents the most effective way to do it. Yet, these anchors should be characterized by a frequency selectivity that inhibits the propagation of acoustic waves to prevent any undesired acoustic leakage. This is key in fact to reduce R_{th} while preserving a high- Q_s . In the next section, we will explain how and why a set of two AMRs placed along the lateral sides of CMRs allows to meet this need. Also, we will show that AMRs offer significant advantages compared to classic MRtopologies [41].

B. Acoustic Metamaterials-based Reflectors

Inspired by electromagnetic (EM) metamaterials, AMs have recently attracted interest from several research groups seeking novel ways to re-engineer acoustic devices [42]-[53]. AMs gained traction by taking advantage of unique surface features to manipulate the dispersion and reflection of acoustic waves propagating along the solid/fluid interface [42], [45], [47]. More recently, the use of AMs has been proposed towards novel ultrasonic frequency selective devices [43], [44], [48], [50]–[52], [54]. A common feature of all these prior works is the attempt to leverage the exotic dispersion features of AMs to generate passbands and stopbands for acoustic wave manipulation. Similarly, in this work, we have explored the adoption of AMRs to generate stopbands that can help tackle the design challenge introduced in Section II-A. Like other AMs-based structures previously demonstrated by our group, AMRs are formed by a forest of piezoelectric rods built on a thin plate. Both such plate and the rods are attained by partial-etching the same AlScN plate used as active material in the CMRs' body. Figure 1-a describes the structure of a unit-cell of AMRs, which is formed by an unpatterned bottom Pt-layer underneath a corrugated AlScN film. AMRs are directly built along the lateral sides of a CMR by cascading a chain of AMRs' unitcells, as shown in Figure 1-b,c where both AMRs' crosssectional and top views are presented. As explained above, our goal is to maintain CMRs' lateral connections to the substrate in order to conduct the heat away from the plate while simultaneously constraining the acoustic energy in the active region (Figure 1-c). To verify AMRs' ability to inhibit the

propagation of the contour-mode excited by CMRs, one could directly investigate AMRs' wave-propagation characteristics. In this regard, Tzung-Chen Wu et al. analyzed the Lamb wave dispersion of a similar grooved structure in [50], and found that the topology added by rods or pillars that are comparable or even thicker than their supporting plate can change dramatically the velocity of the Lamb modes propagating along the plate. Such hybridization-process can leads to the generation of multiple Bragg bandgaps (BGs) in the acoustic transmission spectrum relative to incident longitudinal modes exhibited by such corrugated AMs-based structure. Also, such BGs become wider as thicker rods are used due to a phenomenon of mode-coupling involving multiple Lamb modes. Given such intriguing acoustic dispersion features, we first recurred to a Finite Element Model (FEM) to verify whether AMRs placed along the lateral sides can really generate large BGs constraining the vibration produced by CMRs along their lateral direction (Figure 3). During this FEM investigation, ten CMR-pairs characterized by different IDT pitches (W_p) labeled as P_1 - P_{10}) were defined. In each pair, one device (labeled as CMR^{AM}, Figure 3-c,d) was implemented with AMRs formed by seven unit-cells with the same numerically optimized geometry used in our experiments, while the other (labeled as CMR^{CNV}, Figure 3-a,b) used stress-free lateral boundaries. We report in Figure 3-a the admittance response of the simulated CMR^{CNV}-devices, each one having a different f_{res} -value set by its IDT pitch $[W_p]$ is tuned from 6 μ m (P_1) to 15 μ m (P_{10})]. In Figure 3-b, examples of the at-resonance total-displacement modeshapes are reported for the CMRCNVdevices with W_p respectively equal to P_2 , P_5 and P_9 . The admittance responses for CMR^{AM}-devices employing the same W_p -values used for the analysis of the CMR^{CNV}-devices are also reported in Figure 3-c. Comparing Figure 3-c against Figure 3-a, it is easy to notice that the CMR^{AM}-devices do not show any strong resonances for frequencies below 280 MHz, contrary to the CMR^{CNV}-devices. Yet, the CMR^{AM}devices show clear responses when their resonance falls into the 280-550 MHz range. In order to understand the origin of such a frequency-selective electrical response, it is useful to look at the at-resonance total displacement modeshapes relative to two CMRAM-devices, with resonance frequencies below and above 280 MHz respectively. For this purpose, we report in Figure 3-d different total-displacement modeshapes for the CMR^{AM}-devices with W_p equal to P_2 and P_9 . Evidently, the CMR^{AM}-device with W_p equal to P_9 exhibits a rapidly decaying displacement profile along AMRs' length, thus showing negligible anchor losses. In contrast, the CMR^{AM}-device with W_p equal to P_2 shows a significant displacement along the AMRs' length, justifying the presence of unsustainable anchor losses that ultimately render the device's admittance almost undetected. The cause of such a difference has been studied through FEM by simulating the acoustic transmission (T) frequency-response of the same AMR-structure used by the analyzed CMR^{AM}-device when considering a longitudinal wave incident upon one of AMR's lateral sides. Interestingly, as shown in Figure 3-e,f, we verified that a region of zerotransmission exists covering the entire 280-550 MHz range, thus explaining the ability to confine the acoustic energy

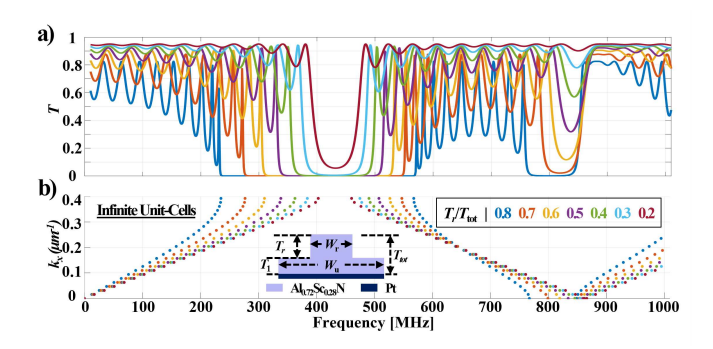


Fig. 4. a) Plot of the FEM-extracted transmission of the AMRs used in Figure 3 vs. frequency, when varying the thickness of the rods (T_r) ; b) Plot of the contour-mode's k_x versus frequency for AMRs used in Figure 3 and for the same T_r values used during the extraction of (a).

within their cavity that all CMR^{AM}-devices operating within such frequency range exhibit. In addition, another narrower zero-transmission frequency range exists, covering the ~800-850 MHz band. A large transmission is instead found across the remaining portion of the analyzed spectrum. A set of total-displacement modeshapes extracted from this latter analysis is provided in Figure 3-f, showing the total pressure distribution for two different frequencies of the incident wave. Evidently, when an incident acoustic wave has a frequency falling out of the two zero-transmission bands, it can propagate through the AMR. Differently, when the incident wave has a frequency included in such bands, it cannot propagate along the AMR, decaying exponentially along its length.

In order to identify the origin of the AMR's zerotransmission bands, an eigenstudy has been performed through FEM by using one AMR's unit-cell and by applying Floquet periodic conditions (FPCs) along its lateral boundaries. The AMR's computed 1-dimensional Bloch diagram within the first Brillouin zone (positive half) is shown in Figure 3g,h, capturing the wavevector (k_x) of the contour-mode vs. frequency. Evidently, this analysis confirmed that the two zero-transmission bands found in the previous acoustic FEMinvestigation of the considered AMR-structure originate from two acoustic BGs that cover exactly the same bands occupied by the zero-transmission regions in Figure 3-e. As already mentioned, another feature that emerged from this FEM investigation is the existence of a second BG, centered around twice the center frequency of the first one. In line with what already observed in [50], the origin of such a second BG is to be attributed to the rods, which generate new regions of inhibited propagation when their thickness is comparable or higher than the thickness of the supporting plate.

This has been confirmed by simulating through FEM T and k_x vs. frequency for increasing rod-thicknesses (T_r , see Figure 4) and when assuming the same in-plane AMR's unitcell geometry considered in Figure 3. Evidently, as the ratio of T_r to the thickness of AMR's AlScN plate (T_1) increases above ten percent, the main AMR's BG starts widening and the second and narrower BG starts forming. We speculate that the near 2:1 correlation between the center frequencies of the identified BG is to be attributed to an elastic energy storing

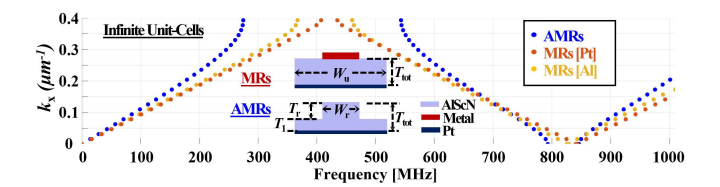


Fig. 5. Comparison between the trends of the contour-mode's k_x vs. frequency for AMRs (in blue), for MRs made of aluminum (in yellow) and for MRs made of platinum (in red).

effect becoming more significant as larger corrugations of the AlScN layer are formed. It is worth mentioning that a similar effect occurs in the MRs used by Surface Acoustic Wave (SAW) resonators operating at frequencies lower than the cut-off frequency for BAW-propagation. In such a scenario, in fact, MRs exhibit a total-reflection at twice the fundamental Bragg-frequency.

C. AMRs vs. Planar Metal Reflectors

While in the previous section we have described the operational principles of AMRs and discussed the origin of AMRs' BGs, it is natural to wonder how AMRs' performance compare to those of MRs. Historically, MRs have been widely used as acoustic reflectors for SAW resonators and transversal filters. They are formed by gratings of metallic strips that create a spatial modulation of the acoustic impedance (Z_{ac}) along the SAW propagation direction. Such a Z_{ac} -modulation produces a BG that ultimately inhibits the lateral propagation of Rayleigh waves along MRs' width.

As proven in [41], MRs can also be used along the lateral sides of AlN Lamb wave resonators to avoid etching their sides. Yet, the perturbation of the Lamb modes' dispersion properties caused by the use of MRs can be significantly different from the one generated by AMRs. Therefore, it is important to compare AMRs' and MRs' performance with respect to their ability to reflect the acoustic energy produced by CMRs and to favor a heat-flow along the lateral direction. In particular, two key metrics need to be considered when comparing such two reflector-structures: the fractional width of their widest BG and their minimum size to ensure a strong enough confinement of the acoustic energy and, consequently, to maximize Q_s . In order to compare AMRs vs. MRs, we relied on a set of FEM simulations. First, the dispersion curve for the contour-mode has been extracted when considering a MR formed by a 120 nm-thick aluminum layer (e.g., the same top-metal thickness and material used in our experiments) and having the same pitch used by the AMR considered in Figure 3. Evidently (Figure 5), AMR's widest BG has a bandwidth that is more than twice the size of the analyzed MRs' BG. This has two crucial practical consequences. First, when using AMRs as lateral anchors of CMRs they ensure performance that are less sensitive to undesired process-variations, which often cause shifts in the center frequency of the BG with respect to the originally targeted one. Second, the same pair of AMRs can be used to confine the acoustic vibration produced by a large pool of CMRs with different resonance frequencies.

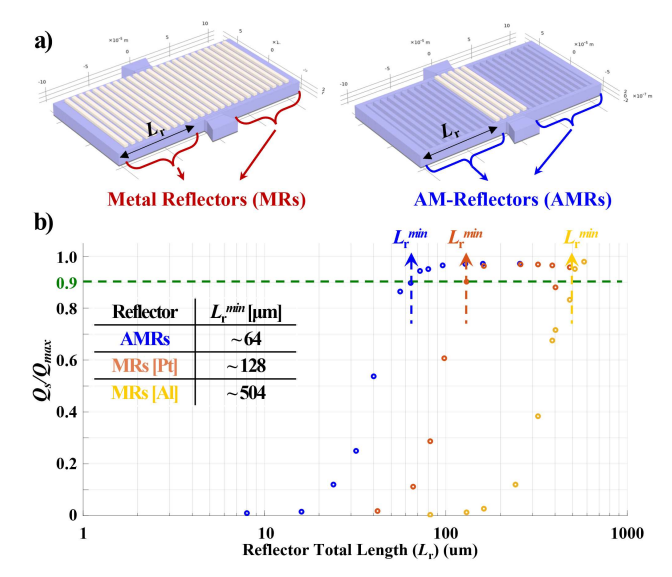


Fig. 6. a) 3D Schematic view of two CMRs, one using MRs along its lateral sides and the other using AMRs; b) plot of the simulated Q_s vs. the lateral length (L_r) of each adopted reflector for: in blue- a CMR AM using the same optimized unit-cell geometry used in Figure 3; in red- a CMR using optimized MRs made of platinum; in yellow- a CMR using optimized MRs made of aluminum. The plotted Q_s -values are normalized to an arbitrarily selected maximum value which was set to 10000 in our FEM simulation. The L_r^{min} value for each of the investigated topologies is also reported in the inset.

Obviously, this is important as it simplifies the complexity of the fabrication process required to manufacture multiple CMR^{AM}-devices with different resonance frequencies on the same wafer.

Another FEM simulation was run to estimate the minimum size (L_r^{min}) of AMRs and MRs when used as lateral anchors in CMRs (Figure 6). In order to find $L_{\rm r}^{\rm min}$, we extracted the normalized distribution of the achievable Q_s (normalized to an arbitrarily chosen intrinsic value, Q_{max} , set to 10,000 in our FEM simulation) vs. the size of the AMRs or MRs used by a CMR to minimize the acoustic energy leakage. In this analysis, the CMR's f_{res} -value (\sim 443 MHz) was assumed to be included in both the BGs formed by our analyzed AMR- and MR-structures. Then, we identified L_r^{min} as the $L_{\rm r}$ -size ensuring normalized $O_{\rm s}$ -values equal to 0.9. For a fair comparison, MRs formed by Pt or Al were also considered here. It is worth mentioning that using aluminum to form MRs for CMRs is practically easier since CMRs generally use Al top-IDTs and no additional fabrication steps would be needed to build the MRs. However, Al offers relatively low values of reflectivity when placed on AlScN, thus being not the best material to use when targeting a MR-design. In contrast, platinum offers a significantly larger reflectivity when placed on AlScN films. Yet, the use of platinum to form the top-IDT of CMRs is not ideal due to the higher thermoelastic and ohmic dissipations that CMRs' Pt IDTs cause. Excitingly, our simulation clearly shows that L_r^{min} is significantly lower for AMRs than for MRs made of Pt or Al. Therefore, we can conclude that AMRs provide a more compact solution than MRs. This generates two key advantages. First, CMR^{AM}devices can be smaller than CMRs using MRs. Secondly and

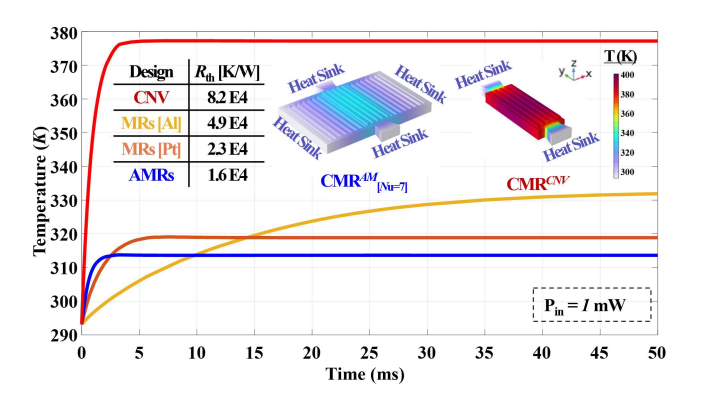


Fig. 7. A 3D-FEM study for the extraction of $R_{\rm th}$ for CMR^{CNV} (in red), CMR^{AM}_{Nu=7} (in blue) and for CMRs using optimized aluminum (in yellow) and platinum (in orange) MRs along their sides. For these two last cases we considered a length for the MRs equal to the corresponding $L_r^{\rm min}$ values found in Figure 6. The extraction of $R_{\rm th}$ for all these devices passed through the evaluation of the average temperature originated in their suspended portion when applying a 1 mW power in their active regions and after setting heat-sinks at the outer edges of all the anchors. The extracted values of $R_{\rm th}$ for all the considered cases is reported.

most importantly, due to their more compact size with respect to MRs, AMRs generate a shorter path for the heat generated into CMRs' active region upon vibration to flow into the substrate. This results into a lower R_{th} and, consequently, in lower thermal nonlinearities and higher power handling. In order to demonstrate this feature, we numerically computed R_{th} for a CMR^{AM}-device using the optimum number of unitcells based on the calculated $L_{\rm r}^{\rm min}$. $R_{\rm th}$ was also computed for two corresponding CMRs with the same design of the active region used by the CMR^{AM}-device but relying on Pt and Al MRs, optimally-sized based on the calculated corresponding $L_{\rm r}^{\rm min}$ values found in Figure 6. Finally, as a reference, we computed R_{th} for a conventional CMR suspended exclusively through the y-anchors. For all these calculations, R_{th} was determined following Eq. 1 and by using the results of ad-hoc 3D-FEM thermal simulations predicting both the thermal time constant (τ_{th}) and the thermal capacitance (C_{th}) of the devices under-study. Evidently, among all the investigated devices, the CMR^{AM}-device shows the lowest R_{th} .

$$\tau_{\rm th} = R_{\rm th} \cdot C_{\rm th} \tag{1}$$

It is worth to emphasize that the identification of $R_{\rm th}$ is particularly important as it allows to predict which devices in a pool of devices are expected to be more or less affected by thermal nonlinearities. In fact, the nonlinear Duffing coefficient ($\alpha_{\rm A-f}$ [14]) capturing the distortion of CMRs' admittance response caused by thermal nonlinearities is directly proportional to $R_{\rm th}$. Thus, regardless of which lateral anchoring strategy is used to achieve the highest possible quality factor value, the thermal linearity of a CMR will be ultimately set by $R_{\rm th}$.

III. EXPERIMENTS AND ANALYSIS

To validate the new reported AlScN CMR^{AM}-design using AMRs, we built and tested six sets of lateral-field-excited

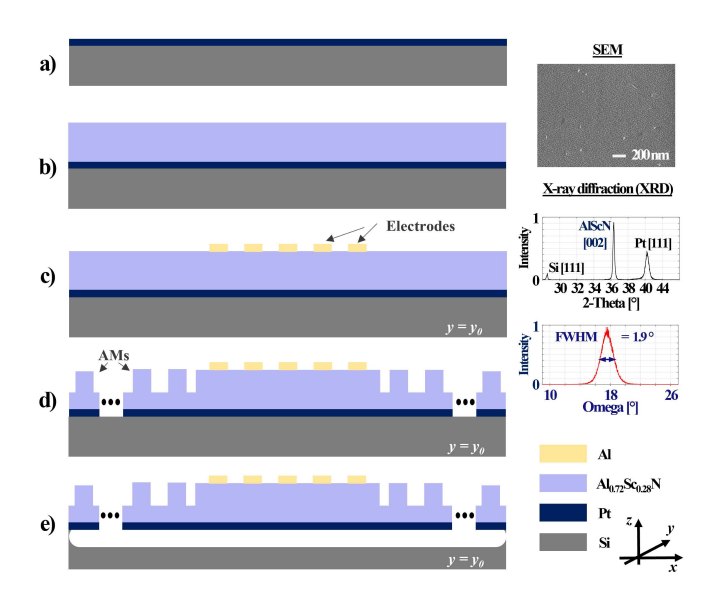


Fig. 8. Fabrication flow used to build all the devices reported in this work. a) Sputtering deposition of 5 nm/60 nm Ti/Pt on top of Si; b) A reactive co-sputtering of Al and Sc in a N_2 atmosphere under 350 °C to form the Al_{0.72}Sc_{0.28}N film; c) Sputtering and lift-off steps to create the Al IDTs; d) Partial Al_{0.72}Sc_{0.28}N-etch using ICP-RIE and a patterned SiO_2 layer as a hard mask; e) the remaining portions of SiO_2 are removed by dry-etching and the devices are released by an isotropic XeF_2 Si-etch. A top-view SEM picture and XRD 2-theta scan and Omega scan of the Al_{0.72}Sc_{0.28}N film are also shown, to observe the AlScN film's low density of abnormally oriented grains (AOGs), as well as its good crystallinity resulting into a the rocking curve with 1.9° Full-Width-Half-Maximum (FWHM).

(LFE) Al_{0.72}Sc_{0.28}N CMRs with identical active regions, material composition and y-anchors' width. In this study six different lateral anchoring strategies were explored. One configuration (CMR^{CNV}) consists in a regular CMR-design with lateral sides fully-etched to form stress-free boundaries. Another configuration (CMRCTL) was designed with the AlScN plate un-etched along the CMR's lateral sides. The four remaining configurations (CMR^{AM}_{Nu=1,3,5,7}) were designed with AMRs along the CMRs' sides formed by 1, 3, 5 and 7 unit-cells respectively, and with an identical numerically optimized unitcell geometry ($T_r = 350 \text{ nm}$, $W_r = 4 \mu\text{m}$, $W_u = 8 \mu\text{m}$). It is worth emphasizing that the unit-cell geometry we used for our experiments is the same we relied on in the simulations we reported for the $CMR^{AM}_{Nu=7}$ considered in Figure 3. All the devices were fabricated on the same wafer by using the fabrication process summarized in Figure 8. In particular, starting from a Si-substrate, we deposited (and patterned under the pads) a 5 nm/60 nm Ti/Pt layer (Figure 8-a). Then, we deposited a 500 nm Al_{0.72}Sc_{0.28}N film (Figure 8-b) by cosputtering Al and Sc at 350 °C in a nitrogen plasma. The achieved effective concentration of Sc-doping was controlled by individually tuning the power levels on the Al- and Sctargets. Next, a room-temperature sputtering and lift-off step was performed to pattern a 100 nm-thick Al layer, forming the IDTs of all CMRs under-investigation (Figure 8-c). Later, we deposited a 200 nm-thick Au layer to form the electrical routing traces and probing pads (this step is not shown in Figure 8). Then, a SiO_2 -layer was deposited via Plasma Enhanced Chemical Vapor Deposition (PECVD) and patterned

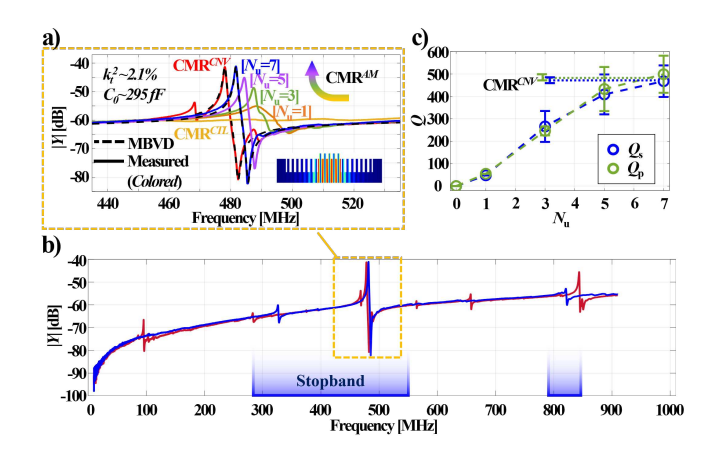


Fig. 9. Measured and fitted admittance responses of the best measured devices for all the investigated CMR-configurations; a) shows the admittance magnitude (|V|) for CMR^{CNV}, CMR^{CTL} and CMR^{AM} [1,3,5,7] within a span ranging from 435 MHz to 535 MHz; b) measured wide-span admittance response for the best CMR^{CNV} and CMR^{AM}_{Nu=7} tested in this work; c) Measured trends of $Q_{\rm s}$ and $Q_{\rm p}$ vs. the number of adopted unit-cells for CMR^{AM} [1,3,5,7] and CMR^{CTL}. The $Q_{\rm s}$ and $Q_{\rm p}$ values exhibited by CMR^{CNV} are also reported.

through Ion Coupled Plasma Reactive Ion Etching (ICP-RIE) to create an hard-mask for etching the Ti/Pt/Al_{0.72}Sc_{0.28}N stack and open the release pits (this step is also not shown in Figure 8). After the release pits were created, a second patterning of the same SiO_2 -layer was performed to generate the hard-mask required to form AMRs' rods (Figure 8-d). Finally, the remaining SiO_2 was removed through dry-etching and all devices under-investigations were released by an isotropic Sietch in XeF_2 , as shown in Figure 8-e. A top-view scanning electron microscopy (SEM) picture and an X-ray diffraction (XRD) 2-theta and Omega scan of the Al_{0.72}Sc_{0.28}N film are shown in the right inset of Figure 8 to demonstrate the low density of abnormally oriented grains (AOGs) and the good crystallinity we were able to achieve for our Al_{0.72}Sc_{0.28}N film. A SEM picture of CMR^{AM}_{Nu=7} is shown in Figure 1-c.

After building the devices, we measured their admittance responses. The measured admittance magnitude (|Y|) for the best devices tested for each analyzed configuration is shown in Figure 9. In particular, Figure 9-a shows |Y| from 435 MHz to 535 MHz, thus within the widest BG of the adopted AMRs (see Figure 3-g). The red and yellow curves correspond to the responses of CMR^{CNV} and CMR^{CTL}. The additional four curves from the measured CMR^{AM}_{Nu=1,3,5,7} are reported in orange, green, purple and blue, respectively. Evidently, we observe the at-resonance admittance magnitude to proportionally grow with the adopted number of unit-cells, indicating an increase of Q_s . Not surprisingly, even the quality factor (Q_p) exhibited by CMR^{AM}_{Nu=1,3,5,7} at the parallel resonance frequency shows an increase vs. the number of unit-cells. In fact, the Q_p -value of any CMR generally matches closely to the CMR's mechanical (e.g., unloaded) quality factor ($Q_{\rm m}$) and it is mainly limited by anchor losses for CMRs operating below 1 GHz [13]. The measured trends of Q_s and Q_p vs. the number of unit-cells $(e.g., N_u)$ is reported in Figure 9b. This trend has been attained by testing and averaging the

TABLE I
MEASURED ELECTROMECHANICAL PERFORMANCE FOR ALL THE BUILT
CMR-CONFIGURATIONS.

Device	$Q_{\rm s}$		Q_{p}		k_t^2	FoM
	AVE	STE^1	AVE	STE ¹	κ_t	FOM
CMR ^{CNV}	409	37.3	415	33.1	0.02	8.2
CMR^{CTL}	0	-	0	-	-	-
$CMR^{AM}_{Nu=1}$	48	0.7	54.5	0.4	-	-
$CMR^{AM}_{Nu=3}$	266	69.0	246.3	19.8	0.02	5
$CMR^{AM}_{Nu=5}$	409.7	89.1	433.3	98.2	0.016	6.5
$CMR^{AM}_{Nu=7}$	468	70.5	499	81.5	0.02	9.4

¹ Standard errors (STE) were also computed for the measured Q_s and Q_p values relative to each configuration tested in this work. The same STE values are shown in Fig. 9-c as error bars.

measured quality factor values relative to at least three devices for each configuration. Also, the quality factor values relative to N_u equal to zero in Figure 9-b refer to the ones of CMR^{CTL}, whereas the Q_s - and Q_p -values of CMR^{CNV} are indicated with green and blue dashed lines respectively. Interestingly, we found CMR^{AM}_{Nu=7} to exhibit even higher quality factor values than CMR^{CNV}. We speculate that such boosted performance may be attributed to $CMR^{AM}_{Nu=7}$'s lower anchor losses along the y-direction than CMR^{CNV} . Such a loss-reduction may be enabled by a weaker mode-conversion experienced by CMR^{AM}_{Nu=7} along its not straight partially-etched lateral sides with respect to CMR^{CNV} [12]. Finally, a wider frequency-span for |Y| is shown in Figure 9-c for CMR^{AM}_{Nu=7} and CMR^{CNV}. Evidently and as expected (Figure 3), while CMR^{CNV} shows strong spurious modes in the passbands of the AMRs used by CMR^{AM}_{Nu=7}, the unique dispersion features of AMRs render these modes almost undetected in $CMR^{AM}_{Nu=7}$. This further confirms that AMRs generate frequency-selective boundary conditions along CMR^{AM}_{Nu=7}'s lateral sides that are reflective only within AMRs' BGs. Finally, we report in Table I a summary of the averaged Q_s , Q_p , k_t^2 , and FoM attained for all tested devices and configurations. It is worth noticing that the adoption of AMRs along the lateral sides of CMR^{AM}devices does not degrade the achievable k_t^2 with respect to what attained by CMR^{CNV}. As a result, the FoM of CMR^{AM}_{Nu=7} also exceeds the one of CMR^{CNV} by nearly fifteen percent.

After completing the electromechanical characterization for the CMR-configurations under investigation, we proceeded with assessing and comparing the thermal linearity of $CMR^{AM}_{Nu=7}$ and CMR^{CNV} . In order to do so, we relied on the extraction of α_{A-f} for both configurations. For a fair comparison between CMR^{CNV} and CMR^{AM}_{Nu=7}, the extraction of α_{A-f} was performed by considering a CMR^{AM}_{Nu=7}device among those we fabricated with nearly the same atresonance admittance magnitude of the best CMR^{CNV}. This choice, in fact, ensures that both devices under-test absorb the same amount of power, which is critical to compare their nonlinear characteristics. During the measurements, the intermediate frequency bandwidth (IFBW) of the input signal was maintained at 50 Hz to make sure that the sampling rate was much slower than the devices' τ_{th} -values, thus ensuring that any measured nonlinear behavior was caused by thermal effects. As expected, we observe the peak of the resonance in the admittance curves bending towards lower frequencies

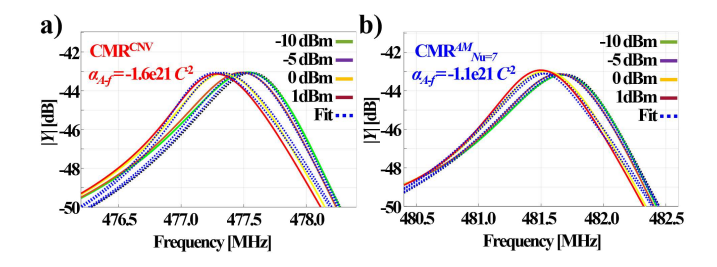


Fig. 10. a) Measured admittance response of the best CMR CNV device tested in this work vs. its input driving power; b) measured admittance response vs. the input driving power for a CMR $^{AM}{}_{Nu=7}$ device with the same at-resonance admittance magnitude than the CMR CNV in (a). The fitted values of α_{A-f} for both devices in (a) and (b) are also shown.

when increasing the input power level (Figure 10-b,c). This represents a key sign of the presence of thermal Duffing nonlinearities[14], [21], which cause a softening-mechanism due to the temperature dependence of the AlScN Young's Modulus. The extraction of α_{A-f} was performed by relying on an equivalent nonlinear-MBVD (Modified-Butterworth Van Dyke, [3]) model, following the methodology discussed in [14]. Such a model replaces the conventional linear motional capacitance ($C_{\rm m}$) of the resonator under-investigation with a charge-dependent one ($C_{\rm m}(q)$) defined in Eq. 2 as:

$$C_{\rm m}(q) = C_{\rm m} \cdot (1 - \alpha_{\rm A-f} \cdot q^2) \tag{2}$$

where q is the motional charge. Then, α_{A-f} was found by fitting the measured nonlinear admittance responses for both devices at different input powers. α_{A-f} was found to be -1.6E21 C^{-2} for CMR^{CNV} and -1.1E21 C^{-2} for CMR^{AM}_{Nu=7}. The fact that the magnitude of α_{A-f} is significantly lower for CMR^{AM}_{Nu=7} confirms our expectations and proves that CMR^{AM}_{Nu=7} suffers less from thermal nonlinearities than CMR^{CNV}.

IV. CONCLUSION

We reported on the first Al_{0.72}Sc_{0.28}N CMR relying on a pair of acoustic metamaterials-based reflectors (AMRs) to laterally anchor the device along its main vibrational direction. We observed that the use of AMRs enables $\sim 15\%$ improved quality factors with respect to conventional CMR designs that rely on fully-etched lateral sidewalls to define the resonant cavity. Moreover, we showed that using AMRs along the lateral sides of CMRs makes it possible to lower the thermal nonlinearities of CMRs. Such unique features, enabled by AMRs, make the CMR-designs reported for the first time in this work a compelling alternative to any prior designs, granting improved electromechanical performance and power handling. In fact, the best device using AMRs that we measured in this work shows a \sim 32% reduction of the Duffing nonlinear coefficient and a ~15% improved figure-of-merit (FoM) with respect to its conventional counterpart. While in this work we have shown how using AMRs can be key to attain future higher performance and more linear filters and oscillators based on AlScN CMRs, we strongly believe that their adoption can be also crucial to improve the performance of other resonator technologies, relying on AlScN or even on other piezoelectric materials available today.

ACKNOWLEDGEMENT

This work was supported by the National Science Foundation (NSF) through the CAREER award (2034948). The authors would like to thank the staff of the George J. Kostas Nanoscale Technology and Manufacturing Research Center, Northeastern University; and the Center for Nanoscale Systems, Harvard University, for their assistance in the device fabrication.

References

- [1] Y. Liu, Y. Cai, Y. Zhang, A. Tovstopyat, S. Liu, and C. Sun, "Materials, Design, and Characteristics of Bulk Acoustic Wave Resonator: A Review," en, *Micromachines*, vol. 11, no. 7, p. 630, 2020. DOI: 10.3390/mi11070630.
- [2] R. C. Ruby, P. Bradley, Y. Oshmyansky, A. Chien, and J. D. Larson, "Thin film bulk wave acoustic resonators (FBAR) for wireless applications," in 2001 IEEE Ultrasonics Symposium. Proceedings. An International Symposium (Cat. No.01CH37263), vol. 1, 2001, 813–821 vol.1. DOI: 10.1109/ULTSYM.2001.991846.
- [3] G. Piazza, P. J. Stephanou, and A. P. Pisano, "Piezoelectric Aluminum Nitride Vibrating Contour-Mode MEMS Resonators," en, *Journal of Microelectromechanical Systems*, vol. 15, no. 6, pp. 1406–1418, 2006. DOI: 10.1109/JMEMS.2006.886012.
- [4] G. Piazza, P. J. Stephanou, and A. P. Pisano, "Single-Chip Multiple-Frequency ALN MEMS Filters Based on Contour-Mode Piezoelectric Resonators," *Journal of Microelectromechanical Systems*, vol. 16, no. 2, pp. 319–328, 2007. DOI: 10.1109/JMEMS.2006.889503.
- [5] C. Zuo, J. Van Der Spiegel, and G. Piazza, "1.05-GHz CMOS oscillator based on lateral- field-excited piezoelectric AIN contour- mode MEMS resonators," *IEEE Transactions on Ultrasonics, Ferroelectrics, and Frequency Control*, vol. 57, no. 1, pp. 82–87, 2010. DOI: 10.1109/TUFFC. 1382
- [6] C. C. W. Ruppel, "Acoustic Wave Filter Technology—A Review," *IEEE Transactions on Ultrasonics, Ferroelectrics, and Frequency Control*, vol. 64, no. 9, pp. 1390–1400, 2017. DOI: 10.1109/TUFFC.2017.2690905.
- [7] Y. Yu, G. Michetti, A. Kord, et al., "Highly-Linear Magnet-Free Microelectromechanical Circulators," *Journal of Microelectromechanical Systems*, vol. 28, no. 6, pp. 933–940, 2019. DOI: 10.1109/JMEMS. 2019.2947903.
- [8] A. Gao, K. Liu, J. Liang, and T. Wu, "AIN MEMS filters with extremely high bandwidth widening capability," en, *Microsystems & Nanoengineering*, vol. 6, no. 1, pp. 1–11, 2020. DOI: 10.1038/s41378-020-00183-5
- [9] G. Piazza, P. J. Stephanou, and A. P. Pisano, "One and two port piezoelectric higher order contour-mode MEMS resonators for mechanical signal processing," en, *Solid-State Electronics*, Special Issue: Papers Selected from the 36th European Solid-State Device Research Conference - ESSDERC'06, vol. 51, no. 11, pp. 1596–1608, 2007. DOI: 10.1016/j.sse.2007.09.037.
- [10] C. Zuo, N. Sinha, J. Van der Spiegel, and G. Piazza, "Multifrequency Pierce Oscillators Based on Piezoelectric AlN Contour-Mode MEMS Technology," *Journal of Microelectromechanical Systems*, vol. 19, no. 3, pp. 570–580, 2010. DOI: 10.1109/JMEMS.2010.2045879.
- [11] M. Rinaldi, C. Zuniga, C. Zuo, and G. Piazza, "Super-high-frequency two-port AlN contour-mode resonators for RF applications," *IEEE Transactions on Ultrasonics, Ferroelectrics, and Frequency Control*, vol. 57, no. 1, pp. 38–45, 2010. DOI: 10.1109/TUFFC.2010.1376.
- [12] J. Segovia-Fernandez, M. Cremonesi, C. Cassella, A. Frangi, and G. Piazza, "Experimental study on the impact of anchor losses on the quality factor of contour mode AIN resonators," in 2013 Transducers & Eurosensors XXVII: The 17th International Conference on Solid-State Sensors, Actuators and Microsystems (TRANSDUCERS & EUROSENSORS XXVII), 2013, pp. 2473–2476. DOI: 10.1109/Transducers.2013.6627307.
- [13] J. Segovia-Fernandez, M. Cremonesi, C. Cassella, A. Frangi, and G. Piazza, "Anchor Losses in AlN Contour Mode Resonators," *Journal of Microelectromechanical Systems*, vol. 24, no. 2, pp. 265–275, 2015. DOI: 10.1109/JMEMS.2014.2367418.
- [14] J. Segovia-Fernandez and G. Piazza, "Thermal Nonlinearities in Contour Mode AlN Resonators," *Journal of Microelectromechanical Systems*, vol. 22, no. 4, pp. 976–985, 2013. DOI: 10.1109/JMEMS.2013.2252422.

- [15] G. A. Slack, R. A. Tanzilli, R. O. Pohl, and J. W. Vandersande, "The intrinsic thermal conductivity of AIN," en, *Journal of Physics and Chemistry of Solids*, vol. 48, no. 7, pp. 641–647, 1987. DOI: 10.1016/ 0022-3697(87)90153-3.
- [16] K. A. Aissa, N. Semmar, D. D. S. Meneses, et al., "Thermal conductivity measurement of AlN films by fast photothermal method," en, Journal of Physics: Conference Series, vol. 395, no. 1, p. 012 089, 2012. DOI: 10.1088/1742-6596/395/1/012089.
- [17] Z. Cheng, Y. R. Koh, A. Mamun, et al., "Experimental observation of high intrinsic thermal conductivity of AlN," Physical Review Materials, vol. 4, no. 4, p. 044 602, 2020. DOI: 10.1103/PhysRevMaterials.4. 044602.
- [18] M. S. B. Hoque, Y. R. Koh, J. L. Braun, et al., "High In-Plane Thermal Conductivity of Aluminum Nitride Thin Films," ACS Nano, vol. 15, no. 6, pp. 9588–9599, 2021. DOI: 10.1021/acsnano.0c09915.
- [19] C. Zuo, M. Rinaldi, and G. Piazza, "Power handling and related frequency scaling advantages in piezoelectric AlN contour-mode MEMS resonators," in 2009 IEEE International Ultrasonics Symposium, 2009, pp. 1187–1190. DOI: 10.1109/ULTSYM.2009.5441932.
- [20] W. Sahyoun, J.-M. Duchamp, and P. Benech, "Acoustic, piezoelectric, and dielectric nonlinearities of AlN in coupled resonator filters for high RF power levels," *IEEE Transactions on Ultrasonics, Ferroelectrics, and Frequency Control*, vol. 58, no. 10, pp. 2162–2170, 2011. DOI: 10.1109/TUFFC.2011.2065.
- [21] A. Tazzoli, M. Rinaldi, and G. Piazza, "Experimental Investigation of Thermally Induced Nonlinearities in Aluminum Nitride Contour-Mode MEMS Resonators," *IEEE Electron Device Letters*, vol. 33, no. 5, pp. 724–726, 2012. DOI: 10.1109/LED.2012.2188491.
- [22] N. Miller and G. Piazza, "Nonlinear dynamics in aluminum nitride contour-mode resonators," *Applied Physics Letters*, vol. 104, no. 1, p. 014 102, 2014. DOI: 10.1063/1.4861461.
- [23] L. Colombo, A. Kochhar, C. Xu, G. Piazza, S. Mishin, and Y. Oshmyansky, "Investigation of 20% scandium-doped aluminum nitride films for MEMS laterally vibrating resonators," in 2017 IEEE International Ultrasonics Symposium (IUS), 2017, pp. 1–4. DOI: 10.1109/ULTSYM. 2017.8092076.
- [24] A. Lozzi, E. Ting-Ta Yen, P. Muralt, and L. G. Villanueva, "Al0.83Sc0.17N Contour-Mode Resonators With Electromechanical Coupling in Excess of 4.5%," *IEEE Transactions on Ultrasonics, Fer*roelectrics, and Frequency Control, vol. 66, no. 1, pp. 146–153, 2019. DOI: 10.1109/TUFFC.2018.2882073.
- [25] G. Esteves, T. R. Young, Z. Tang, et al., "Al0.68Sc0.32N Lamb wave resonators with electromechanical coupling coefficients near 10.28%," Applied Physics Letters, vol. 118, no. 17, p. 171902, 2021. DOI: 10. 1063/5.0047647.
- [26] V. Moraes, H. Riedl, R. Rachbauer, et al., "Thermal conductivity and mechanical properties of AlN-based thin films," Journal of Applied Physics, vol. 119, no. 22, p. 225 304, 2016. DOI: 10.1063/1.4953358.
- [27] R. Rounds, B. Sarkar, D. Alden, et al., "The influence of point defects on the thermal conductivity of AlN crystals," *Journal of Applied Physics*, vol. 123, no. 18, p. 185 107, 2018. DOI: 10.1063/1.5028141.
- [28] R. L. Xu, M. Muñoz Rojo, S. M. Islam, et al., "Thermal conductivity of crystalline AlN and the influence of atomic-scale defects," *Journal* of Applied Physics, vol. 126, no. 18, p. 185 105, 2019. DOI: 10.1063/1. 5097172.
- [29] Y. Song, C. Perez, G. Esteves, et al., "Thermal Conductivity of Aluminum Scandium Nitride for 5G Mobile Applications and Beyond," en, ACS Applied Materials & Interfaces, vol. 13, no. 16, pp. 19031–19041, 2021. DOI: 10.1021/acsami.1c02912.
- [30] X. Zhao, L. Colombo, and C. Cassella, "Aluminum nitride two-dimensional-resonant-rods," *Applied Physics Letters*, vol. 116, no. 14, p. 143 504, 2020. DOI: 10.1063/5.0005203.
- [31] X. Zhao and C. Cassella, "A Comparative Study on the Performance of Aluminum Nitride Thickness and quasi-Thickness Extensional Mode Resonators," in 2020 IEEE International Ultrasonics Symposium (IUS), 2020, pp. 1–4. DOI: 10.1109/IUS46767.2020.9251735.
- [32] X. Zhao, O. Kaya, M. Pirro, et al., "A 5.3 GHz Al0.76Sc0.24N Two-Dimensional Resonant Rods Resonator With a kt2 of 23.9%," Journal of Microelectromechanical Systems, vol. 31, no. 4, pp. 561–570, 2022. DOI: 10.1109/JMEMS.2022.3178978.
- [33] X. Zhao, O. Kaya, M. Pirro, G. Michetti, L. Colombo, and C. Cassella, "An Ultra-Low Impedance 4.8 GHz Al72Sc28N Resonant Rods Resonator With a Record kt2 of 21.2%," in 2021 IEEE MTT-S International Microwave Filter Workshop (IMFW), 2021, pp. 312–315. DOI: 10.1109/ IMFW49589.2021.9642286.

- [34] X. Zhao and C. Cassella, "Slow Waves in Metamaterial Two-Dimensional-Resonant-Rods (2DRRs) Delay Lines," in 2020 IEEE International Ultrasonics Symposium (IUS), 2020, pp. 1–3. DOI: 10.1109/ IUS46767.2020.9251497.
- [35] O. Kaya, X. Zhao, and C. Cassella, "An Aluminum Scandium Nitride (Al0.64Sc0.36N) Two-Dimensional-Resonant-Rods Delay Line with 7.5% Bandwidth and 1.8 dB Loss," in 2022 IEEE 35th International Conference on Micro Electro Mechanical Systems Conference (MEMS), 2022, pp. 1018–1021. DOI: 10.1109/MEMS51670.2022.9699475.
- [36] O. Kaya, X. Zhao, and C. Cassella, "Frequency Reprogrammable Al0.7Sc0.3N Acoustic Delay Line with up to 13.5 % Bandwidth," in 2022 Joint Conference of the European Frequency and Time Forum and IEEE International Frequency Control Symposium (EFTF/IFCS), 2022, pp. 1–4. DOI: 10.1109/EFTF/IFCS54560.2022.9850681.
- [37] G. Wingqvist, L. Arapan, V. Yantchev, and I. Katardjiev, "Temperature compensation of thin AlN film resonators utilizing the lowest order symmetric lamb mode," in 2008 IEEE Ultrasonics Symposium, 2008, pp. 1207–1210. DOI: 10.1109/ULTSYM.2008.0291.
- [38] C. V. Anderson and K. K. Tamma, "An overview of advances in heat conduction models and approaches for prediction of thermal conductivity in thin dielectric films," *International Journal of Numerical Methods for Heat & Fluid Flow*, vol. 14, no. 1, pp. 12–65, 2004. DOI: 10.1108/ 09615530410511621.
- [39] G. Chen, "Thermal conductivity and ballistic-phonon transport in the cross-plane direction of superlattices," *Physical Review B*, vol. 57, no. 23, pp. 14 958–14 973, 1998. DOI: 10.1103/PhysRevB.57.14958.
- [40] L.-C. Xu, R.-Z. Wang, X. Yang, and H. Yan, "Thermal expansions in wurtzite AlN, GaN, and InN: First-principle phonon calculations," *Journal of Applied Physics*, vol. 110, no. 4, p. 043 528, 2011. DOI: 10.1063/1.3627237.
- [41] V. Yantchev and I. Katardjiev, "Thin film Lamb wave resonators in frequency control and sensing applications: A review," en, *Journal of Micromechanics and Microengineering*, vol. 23, no. 4, p. 043 001, 2013. DOI: 10.1088/0960-1317/23/4/043001.
- [42] Z. Liu, X. Zhang, Y. Mao, et al., "Locally Resonant Sonic Materials," Science, vol. 289, no. 5485, pp. 1734–1736, 2000. DOI: 10.1126/science. 289.5485.1734.
- [43] Y. Tong and T. Han, "Anchor Loss Reduction of Lamb Wave Resonator by Pillar-Based Phononic Crystal," en, *Micromachines*, vol. 12, no. 1, p. 62, 2021. DOI: 10.3390/mi12010062.
- [44] R. Yang, Y. Zhang, J. Qian, and J. E.-Y. Lee, "Effect of Phononic Crystal Orientation on AlN-on-Silicon Lamb Wave Micromechanical Resonators," *IEEE Sensors Journal*, vol. 22, no. 17, pp. 16811–16819, 2022. DOI: 10.1109/JSEN.2022.3192088.
- [45] S. Yin, E. Galiffi, and A. Alù, "Floquet metamaterials," *eLight*, vol. 2, no. 1, p. 8, 2022. DOI: 10.1186/s43593-022-00015-1.
- [46] N. Fang, D. Xi, J. Xu, et al., "Ultrasonic metamaterials with negative modulus," en, Nature Materials, vol. 5, no. 6, pp. 452–456, 2006. DOI: 10.1038/nmat1644.
- [47] Y. Cheng, J. Y. Xu, and X. J. Liu, "Broad forbidden bands in parallel-coupled locally resonant ultrasonic metamaterials," *Applied Physics Letters*, vol. 92, no. 5, p. 051913, 2008. DOI: 10.1063/1.2839401.
- [48] T.-T. Wu, Z.-G. Huang, T.-C. Tsai, and T.-C. Wu, "Evidence of complete band gap and resonances in a plate with periodic stubbed surface," en, *Applied Physics Letters*, vol. 93, no. 11, p. 111 902, 2008. DOI: 10.1063/ 1.2970992.
- [49] M.-H. Lu, L. Feng, and Y.-F. Chen, "Phononic crystals and acoustic metamaterials," en, *Materials Today*, vol. 12, no. 12, pp. 34–42, 2009. DOI: 10.1016/S1369-7021(09)70315-3.
- [50] T.-C. Wu, T.-T. Wu, and J.-C. Hsu, "Waveguiding and frequency selection of Lamb waves in a plate with a periodic stubbed surface," *Physical Review B*, vol. 79, no. 10, p. 104306, 2009. DOI: 10.1103/ PhysRevB.79.104306.
- [51] X. Rottenberg, R. Jansen, P. Verheyen, R. Van Hoof, A. Verbist, and H. Tilmans, "Engineering of acoustic metamaterials with application to MEMS BAW resonators," in 2011 16th International Solid-State Sensors, Actuators and Microsystems Conference, 2011, pp. 930–933. DOI: 10.1109/TRANSDUCERS.2011.5969702.
- [52] E. G. Williams, P. Roux, M. Rupin, and W. A. Kuperman, "Theory of multiresonant metamaterials for A 0 Lamb waves," en, *Physical Review B*, vol. 91, no. 10, p. 104 307, 2015. DOI: 10.1103/PhysRevB.91.104307.
- [53] S. A. Cummer, J. Christensen, and A. Alù, "Controlling sound with acoustic metamaterials," en, *Nature Reviews Materials*, vol. 1, no. 3, pp. 1–13, 2016. DOI: 10.1038/natrevmats.2016.1.
- [54] D. Hatanaka, M. Kurosu, and H. Yamaguchi, "Control of Elastic Waves Using Phonon Waveguides and Phononic Crystals," en, NTT Technical Review, vol. 20, no. 4, pp. 43–48, 2022. DOI: 10.53829/ntr202204fa7.



Xuanyi Zhao (Graduate Student Member, IEEE) received the B.S. degree in applied physics from Xi'an Jiaotong University (XJTU), Xi'an, China, in 2015. He is currently a Ph.D. candidate at the Department of Electrical and Computer Engineering, Northeastern University, Boston, MA, USA. His current research interests include micro acoustic radio frequency (RF) devices based on piezoelectric acoustic metamaterials (AMs). One of his previous journal articles was selected as a featured article by the Applied Physics Letters magazine. He recently

won the Best Paper Award at the IEEE International Frequency Control Symposium (IFCS), Paris, in 2022.



Onurcan Kaya (Graduate Student Member, IEEE) received the B.S. and M.S. degrees in mechanical engineering from Middle East Technical University (METU), Ankara, Turkey, in 2014 and 2017, respectively. He is currently pursuing the Ph.D. degree with the Department of Electrical and Computer Engineering, Northeastern University, Boston, MA, USA. His research interests are the design, fabrication, and characterization of MEMS devices, particularly capacitive resonant sensors, piezoelectric acoustic resonators, piezoelectric acoustic delay elements,

and ferroelectric varactors.



Michele Pirro Michele Pirro received the B.S. degree from Politecnico di Torino, Turin, Italy, in 2013, and the M.Sc. degree in micro- and nanotechnologies from INP Grenoble, France, and Politecnico di Torino in 2015. He received the PhD degree in Electrical Engineering from Northeastern University, in Boston, MA, USA, in 2022. His research focused on time-variant electrical circuits and on the characterization of scandium-doped aluminium nitride for MEMs technology. He has coauthored more than 20 publications in those research

areas. He is currently employed at Skyworks Solutions, Inc., Irvine, CA, USA.



Pietro Simeoni received the B.S. degree in engineering physics and the M.S. degree in nanotechnologies for ICTs from the Politecnico di Torino, Turin, Italy, in 2014 and 2016, respectively, and the Ph.D. degree from Carnegie Mellon University in 2021. Currently, he is with the Electrical and Computer Engineering Department, Northeastern University. His Ph.D. research was focused on airborne ultrasonic communication for low-power wake-up applications. His research focuses on device and systems level development of piezoelectric electromechanical

sensing platforms. He is a 2019 Marsha and Philip Dowd Graduate Fellow.



Jeronimo Segovia-Fernandez (M'15) is an R&D Systems Engineer at Texas Instruments Kilby Labs in Santa Clara (USA). He received his M.S. and B.S. degrees in Industrial Engineering with minor in Electronics from the University of Castilla-La Mancha, Ciudad Real (Spain) in 2008, and his Ph.D. degree in Electrical and Computer Engineering from Carnegie Mellon University, Pittsburgh (USA) in 2015. His main research focus has been on piezoelectric MEMS integrated with analog and radio frequency (RF) circuits for applications related to

wireless communications, timing, sensing, and power management. He has authored and co-authored more than 50 publications in peer-reviewed journals and conference proceedings. He holds 4 patents and 7 patent applications. Dr. Segovia-Fernandez received the Mahboob Khan Outstanding Industry Liaison award from SRC in 2022, won the Best Paper Award at IFCS in Prague in 2013, and 2 of his peer-reviewed journal papers were selected as papers of excellent quality (JMEMS RightNow Papers). He is a Technical Reviewer for several journals (IEEE Sensors, JMEMS, TUFFC, TED and APL) and international conferences (Transducers, IFCS and IEEE Sensors), and volunteers at the IEEE San Francisco-Bay Area (SFBA) MEMS and Sensors Chapter (Chair) and IEEE MEMS Technical Community (Media VP).



Cristian Cassella (Member, IEEE) received the B.S.E. and M.Sc. degrees (Hons.) from the University of Rome Tor Vergata in 2006 and 2009, respectively, and the Ph.D. degree from Carnegie Mellon University in 2015. In 2011, he was a Visiting Scholar with the University of Pennsylvania. In 2015, he was a Post-Doctoral Research Associate at Northeastern University. In 2016, he became an Associate Research Scientist. He is currently an Assistant Professor with the Electrical and Computer Engineering Department, Northeastern University,

Boston, USA. He is the author of 83 publications in peer-reviewed journals and conference proceedings. Two of his peer-reviewed journal articles published on the IEEE Journal of Microelectromechanical Systems (JMEMS) were selected as the Papers of Excellent Quality (JMEMS RightNowPapers), hence being released as open-access. One of his journal articles was chosen as the cover for the Nature Nanotechnology October 2017 Issue. Another one of his journal articles was selected as a featured article by the Applied Physics Letters magazine. He holds five patents and two patent applications in the area of acoustic resonators and RF systems. In 2018, he was awarded by the European Community (EU) the Marie-Sklodowska-Curie Individual Fellowship. In 2021, he was a recipient of the NSF Career Award. He received the Best Student Paper Award at the IEEE International Frequency Control Symposium in 2013, 2021 (with his student), and 2022 (with his student). He is a Technical Reviewer of several journals, such as Applied Physics Letters, IEEE Transactions On Electron Devices, IEEE Transactions on Ultrasonics, Ferroelectric and Frequency Control, IEEE Journal of Microelectromechanical Systems, IEEE Electron Device Letters, Journal of Micromechanics and Microengineering, Journal of Applied Physics, IEEE Sensors Letters, and Review of Scientific Instruments.